

Actin network architecture and elasticity in lamellipodia of melanoma cells

Frank Fleischer¹, Revathi Ananthakrishnan², Stefanie Eckel¹,
Hendrik Schmidt¹, Josef Käs³, Tatyana Svitkina⁴, Volker
Schmidt¹ and Michael Beil⁵

¹Institute of Stochastics, University of Ulm, D-89069 Ulm, Germany, Phone: +49 731 50 23531

²Laboratory of Cell and Computational Biology, Section of Molecular and Cellular Biology, University of California at Davis, Davis, CA-95616, USA, Phone: +1 530 752 2273

³Division of Soft Matter Physics, Department of Physics, University of Leipzig, D-04103 Leipzig, Germany, Phone: +49 341 9732471

⁴Department of Biology, University of Pennsylvania, Philadelphia, PA 19104, USA, Phone: +1 215 898 5736

⁵Department of Internal Medicine I, University Hospital, D-89070 Ulm, Germany, Phone: +49 731 500 24860

E-mail: michael.beil@uni-ulm.de

Abstract. Cell migration is an essential element in the immune response on the one hand and in cancer metastasis on the other hand. The architecture of the actin network in lamellipodia determines the elasticity of the leading edge and contributes to the regulation of migration. We have implemented a new method for the analysis of actin network morphology in the lamellipodia of B16F1 mouse melanoma cells. This method is based on fitting multi-layer geometrical statistical models to electron microscopy images of lamellipodial actin networks. The chosen model and F-actin concentrations are thereby deterministic parameters. Using this approach we identified distinct structural features of layered actin networks in lamellipodia. The mesh size which defines the elasticity of the lamellipodium was determined as 34 and 78 nm for a two-layer network at a total actin concentration of 9.6 mg/ml. These data lead to estimates of the low frequency elastic shear moduli which differ by more than a magnitude between the two layers. These findings indicate an anisotropic shear modulus of the lamellipodium with the stiffer layer being the dominant structure against deformations in the lamellipodial plane while perpendicular to the lamellipodial plane the softer layer will contribute significantly at lower indentations creating a material that is optimal to push forward and to squeeze through narrow spaces.

Keywords ACTIN, CYTOSKELETON, ELASTICITY, LAMELLIPODUM, SPATIAL STATISTICS, TESSELLATION MODELS

1. Introduction

Cell migration proceeds within the context of tissue structures. Thus, motile cells have to overcome the mechanical resistance of the surrounding cells and extracellular matrix by adapting their shape and physical properties (Wolf et al., 2003). The actin filament network can regulate the elasticity of the whole cell body and, consequently, influences cell migration (Beil et al., 2003; Park et al., 2005). The movement of cells starts with a locally confined reorganisation of subcortical cytoplasmic compartments which enables the directed motility of cells (Danuser, 2005; Vallotton et al., 2004; Yamazaki et al., 2003). Formation and protrusion of the leading edge are regulated by the local remodeling of the actin network which consists of at least two morphologically distinct structures: lamellipodia and filopodia with the latter arising from the dendritic actin network of lamellipodia (Pollard and Borisy, 2003; Svitkina et al., 2003). Although simulation models for the formation of actin networks could explain the propulsive activity of lamellipodia (Maly and Borisy, 2001; Mogilner and Oster, 1996), global morphological properties of real actin networks in cells have not been characterized yet. This is mainly due to the fact that most microscopic techniques employed for the imaging of individual actin filaments are two-dimensional (2D), i.e. the three-dimensional (3D) architecture of actin networks is projected into 2D images (Svitkina and Borisy, 1998). Although lamellipodia represent a very thin cytoplasmic compartment (Atilgan et al., 2005), they can contain several superimposed layers of flat actin networks (Small et al., 1995). This topological problem has to be dealt with when extracting structural data and estimating biophysical features from 2D images (MacKintosh et al., 1995; Ananthakrishnan et al., 2006).

The architecture of the cytoskeleton is determined by deterministic as well as stochastic processes which modulate the build-up and remodeling of filament networks. Taking these characteristics into account we have developed a new approach to the morphological analysis of cytoskeletal filament networks (Beil et al., 2006). This method is based on the fitting of statistical geometrical models to cytoskeletal networks with the choice of the specific model and the density of structural components representing deterministic elements. The set of models comprises Poisson-Line tessellations (PLT), Poisson-Voronoi tessellations (PVT) and Poisson-Delaunay tessellations (PDT). From a biological point of view, the PLT model represents a set of randomly positioned filaments whose shape is not influenced by interconnections (Figure 1a). In contrast, both PDT and PVT models describe a network of branched filaments (Figure 1b, c). The PVT model reflects a functionally isotropic pattern of interconnected filaments, whereas the PDT model appears to represent the build-up of major branching points inducing filament arrangements in a few preferred directions. Although these models represent complex topological scenarios, they can be described by a single parameter, i.e. the density of filaments or branching points (Gloaguen et al., 2006). By superimposing a finite number of these 2D geometric models, the variety of structural scenarios can be further extended. Thus, this approach provides

the opportunity to reduce the morphological complexity of cellular filament networks to a small number of parameters. The fitting of these multi-layer models to images of filament networks is performed by comparing the morphological characteristics of both stochastic and real networks in an m -dimensional space (Gloaguen et al., 2006).

A proper architecture of the actin network is a prerequisite for the protrusion of the cytoplasm at the leading edge (Desmarais et al., 2004). To assess the morphology of lamellipodia in a quantitative way, we used the models described above for a structural analysis of actin networks in electron microscopic images of mouse melanoma cells. Based on the specific morphological properties of the leading edge, i.e. flat structure (Atilgan et al., 1995), the geometrical models used in this study assume that the architecture of lamellipodia can be modeled by different layers of flat actin networks. The structural properties of these layers are then used to estimate the elasticity of lamellipodia.

2. Materials and methods

2.1. Specimen preparation and image processing

The mouse melanoma cell line B16F1 was provided by Dr. C. Ballestrem (Weizmann Institute of Science, Rehovot, Israel). Cell culture, specimen preparation and electron microscopy imaging were performed as described by Svitkina et al. (2003). Figure 2 depicts the typical architecture of lamellipodia in these cells.

The superposition of actin filament networks can be regarded as a network of line segments with all endpoints being connected. Thus, a watershed segmentation (Soille, 2003) could be applied for grayscale skeletonization. In the resulting dam structure, each pixel was classified into crosspoints and linepoints. In the next step, this dam structure was compared to the original image. For each dam pixel the grayscale values at the corresponding coordinates are regarded along lines. If the minimum of these values is bigger than a given threshold t the line is kept, otherwise it is discarded. This procedure removes lines which resulted from topological disturbances and do not correspond to actin filaments. Assuming that the image of an actin filament approximates a straight line due to a sufficiently large persistence length, dams are then replaced by straight lines between the two endpoints of the dam. Finally, topological disturbances of the primary segmentation are corrected by merging neighbouring branching points having a distance below a given threshold. This merging is done such that pairs of branching points with a smaller distance to each other are merged first. The final result is a graph structure consisting of nodes and connecting line segments (Figure 3).

2.2. Fitting of tessellation models

With regard to the input data, we consider the characteristics $\lambda_1, \dots, \lambda_4$ that correspond to the mean number of vertices, the mean number of edges, the mean number of meshes, and the mean total length of edges, respectively, always measured with respect to the unit area. The entries of the vector

$$\lambda = (\lambda_1, \dots, \lambda_4)^\top \quad (2.1)$$

are estimated from the graph structure that arises from the original electron microscopy images. To compare a vector of estimated characteristics from the input data with a vector of theoretical mean values a distance measure is needed. In this paper we consider the relative Euclidean distance measure given by

$$d_e(y, z) = \left(\sum_{i=1}^m \left(\frac{y_i - z_i}{y_i} \right)^2 \right)^{1/2}, \quad (2.2)$$

where $y = (y_1, \dots, y_m)^\top$ and $z = (z_1, \dots, z_m)^\top$ denote two vectors with m (in our case 4) entries. Notice that in this context the distance measure does not have a geometrical interpretation, but refers to the distance of two vectors with respect to this measure. In Figure 1 realizations of the three basic non-iterated tessellation models are displayed. For these three realizations the model parameters were chosen such that the mean total length of the edges per unit area of the three different models is equal. The relationships between the four different characteristics $\lambda_1, \dots, \lambda_4$ introduced in 2.1 and the parameter γ of a basic tessellation are known for these types of tessellations (Stoyan et al., 1995; Table 1). Note that for each type of basic tessellation the parameter γ has a different meaning that is explained below. The PLT is induced by a random Poisson line process in the plane. This Poisson line process can alternatively be regarded as a Poisson point process on $\mathbb{R} \times [0, \pi]$ due to the fact that each line is uniquely determined by the signed perpendicular distance to the origin and by the angle in anti-clockwise direction between the orientation vector of the line and the x -axis. The parameter γ_{PLT} represents the mean total length of edges per unit area. The PVT is based on a Poisson point process $X = \{X_n\}$ in the plane with intensity γ_{PVT} representing the mean number of points per unit area. Afterwards Voronoi meshes are constructed with respect to the nuclei $\{X_n\}$ by using the nearest neighbour principle. Finally, the PDT can be generated by a PVT. If a generating PVT is considered and nuclei of these meshes that share a common edge are connected, then a PDT is formed. Hence we obtain that the vertices of a PDT are given by the nuclei of the generating PVT and that an edge of the PDT is always perpendicularly crossing an edge of the generating PVT. Since in the case of Poisson processes almost surely three different points do not lie on one and the same line, the meshes of the PDT are triangles with probability one. The intensity γ_{PDT} denotes the mean number of vertices of the PDT per unit area. These basic tessellations can be used to construct tessellation models that are

more sophisticated by a superposition of n ($n \geq 1$) independent layers (Figure 4). Such a superposed tessellation can of course be the initial tessellation for a further tessellation step. If the superposition is performed once and if we consider PLTs, PVTs and PDTs as possible model classes for the two tessellation layers we end up with at most nine different possible model classes. Notice that a symmetry occurs in the sense that for example a PLT/PVT superposition with parameters γ_0 and γ_1 has the same distribution as a PVT/PLT superposition with parameters reversed. Hence the nine different possible model classes are reduced to six. Notice furthermore that a PLT/PLT superposition is equal in distribution to a basic PLT tessellation, whereas this property is not true for PVT/PVT and PDT/PDT with respect to a PVT and a PDT tessellation, respectively. Mean value formulae for these six different possible superposition models are given in Table 2 (Maier and Schmidt, 2003). Notice that also for superpositions consisting of three or more layers mean value formulae can be derived in a similar fashion. For a three-layer superposition with PLT, PVT and PDT as basic models we obtain seven new possible model classes due to the fact that the 27 original possibilities are reduced by similar effects as for the two-layer superpositions.

2.3. Algorithm summary

The model choice algorithm applied can be summarized as follows. Given an input image, the vector of characteristics $\lambda = (\lambda_1, \dots, \lambda_4)$ is estimated, leading to estimates $\hat{\lambda} = (\hat{\lambda}_1, \dots, \hat{\lambda}_4)$ (see Beil et al. (2006) for details with respect to estimators). By using the relative Euclidean distance measure introduced in 2.2 for each of the six possible superposed tessellation models separately a relative distance function

$$f_{model}(\gamma_0, \gamma_1) = \left(\sum_{i=1}^4 \left(\frac{\hat{\lambda}_i - \lambda_i^{model}}{\hat{\lambda}_i} \right)^2 \right)^{1/2} \quad (2.3)$$

can be constructed, where γ_0 and γ_1 denote the parameters for the two layers of the superposed tessellation. The values λ_i^{model} are then the theoretical model characteristics depending on the choice of the superposed tessellation model and of γ_0 and γ_1 . Then for each model separately an optimal parameter vector is determined; this means a vector (γ_0, γ_1) that minimizes $f_{model}(\gamma_0, \gamma_1)$ for the given model. A model is considered optimal among all possible models if the optimal value $f_{model}(\gamma_0, \gamma_1)$ is minimal with respect to all models. In the given data set instead of investigating single data samples, it is reasonable to investigate mean samples since samples of the same group can be considered to be independent and identically distributed. Here the averaging is performed in an arithmetical sense meaning that a vector of characteristics $(\bar{\lambda}_1, \bar{\lambda}_2, \bar{\lambda}_3, \bar{\lambda}_4)$ is estimated from the n samples by

$$\bar{\lambda}_i = \frac{1}{n} \sum_{j=1}^n \hat{\lambda}_{ij}, \quad (2.4)$$

where $\hat{\lambda}_{ij}$ is the estimated i -th characteristic for the j -th sample. Notice that such an averaging is comparable to the data being measured in a single but much larger sampling window. All software that was developed and used for the image analysis as well as for the model fitting procedure is included in the GeoStoch library which is a Java-based library system (Mayer et al., 2004; <http://www.geostoch.de>).

3. Results

Seven sample regions from different melanoma cells were analysed (Figure 2). Assuming that the samples are independently drawn from one and the same distribution, the analysis of the vector of mean characteristics is comparable to an analysis of a single but larger sampling window. Hence it is important to note that it is not the number of images analysed that is the most important factor for the accuracy of the analysis but the total area that is considered. Here, the total area analysed was $10.91 \mu\text{m}^2$. The total run-time for the computations (including image segmentation) was less than 1 hour.

3.1. Concentration of filamentous actin in the lamellipodium

The total amount of filamentous actin was calculated by measuring the total length of skeleton lines in the images. Note that the accuracy of this method is hardly affected by an overlay of actin filaments from different layers since the skeleton lines have a negligible width and they are mainly orientated orthogonally to the vertical axis. Therefore, assuming that an actin filament with a length of $1 \mu\text{m}$ consists of 370 actin molecules with a molecular weight of 43 kDa (Tang and Janmey, 1996) and that the lamellipodium has a thickness of 200 nm (Atilgan et al., 2005), the concentration of filamentous actin was calculated as 9.6 mg/ml for a measured total length of the skeleton lines of $7.24 * 10^{-2} \text{ nm/nm}^2$.

3.2. Actin network morphology

To obtain objective features of global network architecture, multi-layer tessellation models were fitted to the graphs representing actin filament networks. Tables 3 contains the results of the model fitting procedure. The relative Euclidean distance measure was applied here, but the results do not vary much if other distance measures are applied.

The data of the fitting procedure show that the optimal superposed model is given by a PVT/PDT superposition (Table 3). The fitting of three-layer models resulted in virtually the same model choices as the fitting of two-layer models, i.e. there was one layer with a corresponding γ value of approximately 0.

Note that here the detected distance value is only a technical characteristic in order to determine the optimal tessellation model with respect to a minimal distance of the estimated vector of mean characteristics from images to the vector of theoretical mean characteristics. In particular, it is not possible to transfer this distance to a linear scale, i.e. the distance has only a qualitative not a quantitative meaning. In order to check for the significance of our model decision we also regarded a model fitting to actin networks of the individual sample images. Here, the PVT/PDT model was found to be the optimal model for all 7 individual images as well, having similar optimal parameters compared to the result for the mean sample (data not shown). Therefore, a possible null hypothesis that the data represents a specific model different from PVT/PDT is clearly rejected ($p < 0.01$), under the (natural) assumption that the probability to decide in favor of a PVT/PDT although the data comes from a different model is less than 0.5. This significant decision in favor of the PVT/PDT model for all individual sample images strongly enhances the decision for the case of the mean sample.

Figure 5 depicts a segmented sample image of actin networks and a realization of the corresponding optimal PVT/PDT superposed model. Notice that in general the similarity between the real images of actin networks and the realizations of the optimal model is only given in a structural sense, i.e. with respect to geometric network characteristics, and not imagewise.

With respect to the total segment lengths, the parameters of the optimal model (PVT/PDT) yield a proportion of 69% for the PVT layer and 31% for the PDT layer. Assuming an equal division of the cytoplasmic volume between the two actin network layers, the actin concentrations for the PDT and PVT layers were determined as 13.25 mg/ml and 5.95 mg/ml , respectively.

3.3. Estimation of actin network elasticity

The elastic plateau shear modulus G of an isotropic crosslinked actin filament network can be calculated as (MacKintosh et al., 1995):

$$G = 6k_b T l_p^2 / (l_e^3 \xi^2), \quad (3.1)$$

with l_p being the persistence length of actin filaments ($17 \mu\text{m}$), l_e , the entanglement length and ξ the mean mesh size. Note that 3.1 refers to isotropic 3D networks. Although the actin networks in lamellipodia represent flat structures, this formula can provide a good estimate for G . The entanglement length l_e is defined as the average distance between points along an actin filament that are effectively constrained; for a fully crosslinked network, this is determined by the distance between crosslinks. The

entanglement length is $2.2 \mu\text{m}$ for a 1 mg/ml actin network and scales as concentration $\rho^{-0.4}$ (Käs et al., 1996). The mean mesh size ξ represents the average distance between neighbouring actin filaments. Due to the superposition of filament layers in 2D images of actin networks, ξ cannot be determined directly from these images. Instead, the value of ξ was estimated by the average maximum diameter of circles inscribed into the meshes of simulated networks for each of the two layers (PVT and PDT). The mean mesh size ξ was found to be 34 nm for the PVT layer and 78 nm for the PDT layer. The mean mesh size of an actin network depends on its actin concentration ρ and this relation can be described by (Morse, 1998):

$$\rho = 1/\xi^2. \quad (3.2)$$

Actin concentrations of 13.25 mg/ml and 5.95 mg/ml as determined for the two network layers would result (using 3.2) in a mean mesh size of 44 nm for the PVT layer and 66 nm for the PDT layer. The relative differences between these mesh size values and those obtained above from the simulations are 23% and 18%.

Based on 3.1 and mesh sizes of 34 and 78 nm , the elastic shear modulus G can be calculated as 23.4 kPa for the PVT layer and 0.6 kPa for the PDT layer. This calculation depends on l_e . Due to slack and projection errors, however, it is difficult to determine l_e directly from the images. In view of the mesh sizes of the fitted tessellation models, the values of l_e determined according to Käß et al. (1996) appear to be over-estimates. Thus, the values of G as determined above are probably under-estimates.

The elasticity G as determined above represents the maximum elasticity of a fully crosslinked actin network. However, since actin crosslinks in vivo are only transient, the effect of transient crosslinking on elasticity (G value) needs to be considered. To account for dynamic crosslinking, we have applied a model for transiently partially crosslinked actin networks (Ananthakrishnan et al., 2006b) that determines the elastic shear modulus depending on the concentration of actin and actin crosslinkers, such as α -actinin. This simplified system represents the minimal set of components necessary to establish an elastic network. Adding other proteins such as filamin or Arp2/3 to the model would further approximate the real intracellular scenario but would significantly increase the complexity of the mathematical model. Figure 6 depicts the relationship between the concentration of a representative cross-linker, i.e. α -actinin, and the elastic shear modulus G for the two actin network layers. Note that at low α -actinin concentrations ($< 10 \mu\text{M}$) as detected, for example, in Acanthamoeba (Pollard et al., 2000), the two graphs demonstrate a different shape resulting in a different tuneability of the network elasticity. Independently of the strong tuneability of the mechanical strength of lamellipodial actin networks by the amount of crosslinker present, it becomes clear that the significantly different mesh sizes in the two detected layers result in a very soft and a distinctively stiffer actin layer.

4. Discussion

Directed migration of cells is regulated by remodeling actin networks in lamellipodia (Abraham et al., 1999). Thus, the analysis of actin network morphology provides essential information for assessing the functional characteristics of the leading edge. Due to the small diameter of actin filaments, electron microscopic techniques have to be applied for the visualization of individual filaments (Svitkina and Borisy, 1998; Shao et al., 2006) which is necessary to obtain the structural information required for the analysis of filament network architecture. With the exception of cryoelectron tomography (Medalia et al., 2002), electron microscopy produces 2D images which are projections of 3D cellular structures. Analysing projections of originally 3D filament networks by conventional image analysis techniques would result in a biased estimation of several important network features, e.g. mesh size. The new method presented here is based on the observation that lamellipodia are composed of flat actin networks (Shao et al., 2006). Thus, the models for filament networks applied in this study were confined to superpositions of 2D geometrical models. The three mathematical models (PLT, PVT, PDT) chosen in this study represent a wide variety of different scenarios with respect to the relationship between the density of filaments, branching points and meshes (Table 1). Although these stochastic models cannot be fitted to strictly deterministic topologies, e.g. Arp2/3-mediated branching patterns, they represent actin network features which are pivotal for network elasticity. Moreover, the three models are still mathematically tractable with respect to explicit mean value formulae for geometric characteristics and can easily be simulated. The different ratios between the model characteristics λ_n can be related to biochemical processes regulating actin network synthesis and remodeling which can prefer filament elongation or branching. Based on the same amount of polymerized actin, a network represented by the PVT model contains almost 50 % more meshes and more than 500 % of the branching points in comparison to a network modeled by PDT. In contrast to a PLT network, where the long filaments could be related to formin-mediated processes (Harris et al., 2006), the PVT and PDT models networks describe networks of branched filaments. Realizations of PVT with γ values shown in Table 3, which are dominated by short interconnected filaments, appear to represent an actin network architecture that is mainly regulated by Arp2/3. The PDT model suggests a different balance between elongation and branching processes permitting the occurrence of local anisotropies within the network (Figure 1), which occur, for example, in the early phases of filopodia formation (Svitkina et al., 2003).

The small number of actin filament layers in lamellipodia allowed the detection of almost all individual filaments, although the geometry of filament branching patterns or crosslinks might not have been detected with perfect accuracy. This was compensated for by fitting statistical tessellation models which reflect major structural characteristics of the filament network while taking stochastic variations into account. The comparison of the tessellation models with images of lamellipodia from B16F1

mouse melanoma cells resulted in the detection of the PVT/PDT superposition model as the optimal fit for these actin networks. The consistent selection of this model for all randomly selected sample images emphasizes the existence of a uniform network morphology for this cytoskeletal compartment. A further increase of the number of superposed layers in the model did not yield different model characteristics which strongly suggests that lamellipodia can be modeled best by two different flat actin networks indicating axial asymmetry, i.e. anisotropy. This fits well with previous observations by Ponti et al. (2004), who have shown that the lamellipodium is composed of two distinct actin networks. Furthermore, Attilgan et al. (2005) demonstrated that the observed thickness of lamellipodia can only be achieved by the filament growth proceeding in two dimensions. Theoretical studies on actin networks also suggest that actin filaments in lamellipodia are, in fact, organized in two-dimensional layers (Maly and Borisy, 2001; Kruse et al., 2006). However, other network configurations, e.g. with a more or less continuous transition between different network compartments might exist. Nevertheless, a discrete model consisting of two layers could be a useful tool to assess the axial anisotropy in lamellipodia.

The total concentration of filamentous actin in the lamellipodium was found to be 9.6 *mg/ml* which is within the range of previously measured data (Zigmond, 1993; Pollard et al., 2000). This measurement was based on determining the length of actin filaments in 2D images. Since actin networks in lamellipodia appear to be spatially restricted in 2D (Shao et al., 2006), the calculation of the total filament length by measuring the projection of filaments provides good estimates of actin concentrations. The two-layer model provided an opportunity to analyse the structural properties of different actin network compartments. This analysis revealed that lamellipodia are anisotropic in the axial direction with respect to morphology and actin concentration. This anisotropy might be caused by the attachment of cells to the substratum which imposes specific demands on the lower compartment of the actin network. Alternatively, the axial anisotropy may have been generated through activity of two different actin filament nucleators, Arp2/3 complex and formins, which nucleate branched and linear filaments, respectively. Comparing the density of actin filaments determined for the different layers of the model with the original images (Figure 2), the lower compartment of the the actin network is described by the PVT model whereas the upper compartment is represented by the PDT model. The parameters of the PVT model indicate a more than 10fold increase of the branching point density in comparision to the PDT model. This results in longer filaments at the PDT level, thus, providing a good match with the original image. However, there cannot be a perfect match between individual images and simulated networks, since the fitted models reflect the inherent structure of these network through their global characteristics. Hence, random realisations of these statistical models may cause variations of the position and properties of local filament arrangements. For the purpose of obtaining approximations for individual samples based on these model classes, Bayesian image analysis techniques based on Markov-Chain-Monte-Carlo methods might prove to be

useful (Blackwell and Møller, 2002; Nicholls, 1998).

The low frequency elastic shear modulus of lamellipodia depends on the mesh size of the actin network (MacKintosh et al., 1995). The mesh size of multi-layer networks cannot be determined directly from 2D images. The two-layer model provided the opportunity to estimate mesh sizes of the layers independently. The mesh sizes obtained from model simulations differed only by 18% and 23% from those calculated from actin concentrations (Morse, 1998). This variation may be due to an unequal division of the cytoplasmic space between the two layers of the actin network in our model affecting concentration values. The small differences emphasize the fact that the properties of the fitted model indeed reflect the structural characteristics of multi-layer actin networks. Based on mesh sizes, the PVT and PDT layers of the actin network were found to have an elastic shear modulus of 23.4 kPa and 0.6 kPa , respectively. These estimates describe the elasticity of a fully crosslinked actin network and are within the range of previously measured data for cell elasticity (Ananthakrishnan et al., 2006a). However, the accuracy of these calculations is restricted by various factors the modeling could not account for, e.g. slack in the actin network and interconnections between adjacent actin filament layers. Nevertheless, the differences of the two layers indicates an anisotropy of the elastic properties of the lamellipodium with the stiffer compartment determining the leading edge's ability to push the cell forward and, thus, supporting the leading edge to penetrate soft tissue compartments. The response to small forces perpendicular to the lamellipodium, however, might be determined by the softer compartment modeled by the PDT layer. This provides the cell with enough softness to move through small tissue slits. Thus, the structural differences between the lower and upper compartments of lamellipodia suggest that cells can shift production of actin networks in order to tune elasticity for agility or resistance.

Another mechanism to regulate the elasticity of the leading edge is the occurrence of transient actin crosslinks, e.g. by α -actinin. This provides lamellipodia with a wide range of elasticity to respond to the biophysical demands imposed on them by the mechanical properties of the surrounding tissue compartments. Importantly, the shape of the tuning curve varies between the two layers of the actin network. Thus, the establishment of an asymmetrical actin network architecture in lamellipodia as revealed in this study may enable the lamellipodium to further fine tune its local structural properties without changing actin crosslinker concentrations.

The lamellipodium represents an interface where a variety of signals is translated into movements of cytoplasmic compartments. This goal is achieved by a dynamic remodeling of the actin filament network which is mainly controlled by actin-associated regulatory proteins. The major mechanisms involved are actin polymerization and filament branching (Bear et al., 2003; Mejillano et al., 2004; Pollard and Borisy, 2003). Although these processes appear to be well understood (Mogilner and Oster 1996; Maly and Borisy, 2001), the interactions of signaling pathways resulting in the formation of specific network patterns remain to be determined. The method presented in

this study could be a useful tool to analyse these complex processes.

Acknowledgments

This work was supported by grants from the Deutsche Forschungsgemeinschaft (DFG) to M. Beil (BE 2339/2) and V. Schmidt (SCHM 997/7). T. Svitkina is supported by NIH grant GM 70898. S.Eckel is supported by a DFG grant to the graduate college 1100 at the University of Ulm. We would like to thank the reviewers of this paper for their valuable comments.

- [1] Abraham V. C., Krishnamurthi V., Taylor D. L. and Lanni F. 1999 The actin-based nanomachine at the leading edge of migrating cells. *Biophys J.* 77:1721-1732.
- [2] Ananthakrishnan R., Guck J. and Käs J. 2006a Cell mechanics: Recent advances with a theoretical perspective. *Recent Res. Devel. Biophys* (in press).
- [3] Ananthakrishnan R., Guck J. , Wottawah F., Schinkinger S. , Lincoln B., Romeyke M., Moon T. and Käs J. 2006b Quantifying the contribution of actin networks to the elastic strength of fibroblasts. *J. Theor. Biol.* (Epub ahead of print).
- [4] Atilgan E., Wirtz D. and Sun S. X. 2005 Morphology of the lamellipodium and organization of actin filaments at the leading edge of crawling cells. *Biophys. J.* 89:3589-3602.
- [5] Bear J. E., Svitkina T. M., Krause M., Schafer D. A., Loureiro J. J., Strasser G. A., Maly I. V., Chaga O. Y., Cooper . A., Borisy G. G. and Gertler F. B. 2002 Antagonism between Ena/VASP proteins and actin filament capping regulates fibroblast motility. *Cell.* 109:509-521.
- [6] Beil M., Eckel S., Fleischer F., Schmidt H., Schmidt V. and Walther P. 2006 Fitting of random tessellation models to cytoskeleton network data. *J. Theor. Biol.* 241:62-72.
- [7] Beil M., Micoulet A., von Wichert G., Paschke S., Walther P., Omáry M. B., van Veldhoven P., Gern U., Wolff-Hieber E., Eggermann J., Waltenberger J., Adler G., Spatz J. and Seufferlein T. 2003 Sphingosylphosphorylcholine regulates keratin network architecture and visco-elastic properties of human cancer cells. *Nat. Cell Biol.* 5:803-811.
- [8] Blackwell P. G. and Møller J. 2002 Bayesian analysis of deformed tessellation models. *Advances in Applied Probability* 35, 4-26.
- [9] Danuser G. 2005 Coupling the dynamics of two actin networks-new views on the mechanics of cell protrusion. *Biochem Soc Trans.* 33:1250-1203.
- [10] Desmarais V., Macaluso F., Condeelis J. and Bailly M. 2004 Synergistic interaction between the Arp2/3 complex and cofilin drives stimulated lamellipod extension. *J Cell Sci.* 117:3499-3510.
- [11] Gloaguen C., Fleischer F., Schmidt H. and Schmidt V. 2006 Fitting of stochastic telecommunication network models, via distance measures and Monte-Carlo tests. *Telecommunication Systems* 31:353-377.
- [12] Harris E. S., Rouiller I., Hanein D. and Higgs H. N. 2006 Mechanistic differences in actin bundling activity of two mammalian formins, FRL1 and mDia2. *Journal of Biological Chemistry* 281:14383-14392
- [13] Head D. A., Levine A. J. and MacKintosh F. C. 2003 Deformation of crosslinked semiflexible polymer networks. *Phys. Rev. Lett.* 91:108102.
- [14] Käs J., Strey H., Tang J. X., Finger D., Ezzell R., Sackmann E. and Janmey P. A. 1996 F-actin, a model polymer for semiflexible chains in dilute, semidilute, and liquid crystalline solutions. *Biophys J.* 70:609-625.
- [15] Kruse K., Joanny F., Julicher F. and Prost J. 2006 Contractility and retrograde flow in lamellipodium motion. *Physical Biology* 3:130-137.
- [16] MacKintosh F., Käs J. and Janmey P. A. 1995 Elasticity of semiflexible biopolymer networks. *Phys. Rev. Lett.* 75:4425-4428.
- [17] Maier R. and Schmidt V. 2003 Stationary iterated tessellations. *Advances in Applied Probability* 35:337-353.
- [18] Maly I. V. and Borisy G. G. 2001 Self-organization of a propulsive actin network as an evolutionary process. *Proc. Natl. Acad. Sci. USA* 98:11324-11329.
- [19] Mayer J., Schmidt V. and Schweiggert F. 2004 A unified simulation framework for spatial stochastic models. *Simulation Modelling Practice and Theory* 12:307-326.
- [20] Medalia O., Weber I., Frangakis A. S., Nicastro D., Gerisch G. and Baumeister W. 2002 Macromolecular architecture in eukaryotic cells visualized by cryoelectron tomography. *Science* 298:1209-13.
- [21] Mejillano M. R., Kojima S., Applewhite D. A., Gertler F. B., Svitkina T. M. and Borisy G. G. 2004 Lamellipodial versus filopodial mode of the actin nanomachinery: pivotal role of the filament barbed end. *Cell* 118:363-373.
- [22] Mogilner A. and Oster G. 1996 Cell motility driven by actin polymerization. *Biophys. J.* 71:3030-

- 3045.
- [23] Møller J. 1989 Random tessellations in \mathbb{R}^d . *Advances in Applied Probability* 21:37-73.
 - [24] Morse D. C. 1998 Viscoelasticity of concentrated isotropic solutions of semiflexible polymers: 1. Model and stress tensors. *Macromolecules* 31:7030-7043.
 - [25] Nicholls G. 1998 Bayesian image analysis with Markov chain Monte Carlo and colored continuum triangulation mosaics. *J. Royal Stat. Soc. B* 60:643-659.
 - [26] Park S., Koch D., Cardenas R., Käs J. and Shih C. K. 2005 Cell motility and local viscoelasticity of fibroblasts. *Biophys. J.* 89:4330-4342.
 - [27] Pollard T. D., Blanchoin L. and Mullins R. D. 2000 Molecular mechanisms controlling actin filament dynamics in nonmuscle cells. *Annu. Rev. Biophys. Biomol. Struct.* 29:545-576.
 - [28] Pollard T. D. and Borisy G. G. 2003 Cellular motility driven by assembly and disassembly of actin filaments. *Cell* 112:453-465.
 - [29] Ponti A., Machacek M., Gupton S. L., Waterman-Storer C. M. and Danuser G. 2004 Two distinct actin networks drive the protrusion of migrating cells. *Science* 305(5691):1782-1786.
 - [30] Shao D., Forge A., Munro P. M. and Bailly M. 2006 Arp2/3 complex-mediated actin polymerisation occurs on specific pre-existing networks in cells and requires spatial restriction to sustain functional lamellipod extension. *Cell Motil. Cytoskeleton.* Apr 17; [Epub ahead of print]
 - [31] Small J. V., Herzog M., Anderson K. 1995 Actin filament organization in the fish keratocyte lamellipodium. *J. Cell Biol.* 129:1275-1286.
 - [32] Soille P. 2003 Morphological Image Analysis. Springer, Berlin.
 - [33] Stoyan D., Kendall W. S. and Mecke J. 1995 Stochastic Geometry and its Applications. J. Wiley & Sons, Chichester.
 - [34] Svitkina T. M. and Borisy G. G. 1998 Correlative light and electron microscopy of the cytoskeleton of cultured cells. *Methods Enzymol.* 298:570-592.
 - [35] Svitkina T. M., Bulanova E. A., Chaga O. Y., Vignjevic D. M., Kojima S., Vasiliev J. M. and Borisy G. G. 2003 Mechanism of filopodia initiation by reorganization of a dendritic network. *J. Cell Biol.* 160:409-421.
 - [36] Tang J. X. and Janmey P. A. 1996 The polyelectrolyte nature of F-actin and the mechanism of actin bundle formation. *J. Biol Chem.* 271:8556-8563.
 - [37] Vallotton P., Gupton S. L., Waterman-Storer C. M. and Danuser G. 2004 Simultaneous mapping of filamentous actin flow and turnover in migrating cells by quantitative fluorescent speckle microscopy. *Proc Natl Acad Sci USA.* 101:9660-9665.
 - [38] Wolf K., Mazo I., Leung H., Engelke K., von Andrian U. H., Deryugina E. I., Strongin A. Y., Brocker E. B. and Friedl P. 2003 Compensation mechanism in tumor cell migration: mesenchymal-amoeboid transition after blocking of pericellular proteolysis. *J. Cell Biol.* 160:267-277.
 - [39] Yamazaki D., Suetsugu S., Miki H., Kataoka Y., Nishikawa S., Fujiwara T., Yoshida N. and Takenawa T. 2003 WAVE2 is required for directed cell migration and cardiovascular development. *Nature* 424:452-456.
 - [40] Zigmond S. H. 1993 Recent quantitative studies of actin filament turnover during cell locomotion. *Cell Motil. Cytoskeleton* 25:309-316.

Table 1. Values of λ_1 (mean number of vertices), λ_2 (mean number of segments), λ_3 (mean number of meshes) and λ_4 (mean total length of segments; all measured per unit area) for a given tessellation with respect to λ_4

Tessellation	λ_1	λ_2	λ_3	λ_4
PLT	$\frac{1}{\pi} \lambda_4^2$	$\frac{2}{\pi} \lambda_4^2$	$\frac{1}{\pi} \lambda_4^2$	λ_4
PVT	$\frac{1}{2} \lambda_4^2$	$\frac{3}{4} \lambda_4^2$	$\frac{1}{4} \lambda_4^2$	λ_4
PDT	$\frac{9\pi^2}{1024} \lambda_4^2$	$\frac{27\pi^2}{1024} \lambda_4^2$	$\frac{18\pi^2}{1024} \lambda_4^2$	λ_4

Table 2. Mean-value formulae for one-fold superpositions

	PLT/PLT	PLT/PVT	PLT/PDT
λ_1	$\frac{1}{\pi}(\gamma_0 + \gamma_1)^2$	$\frac{1}{\pi}\gamma_0^2 + 2\gamma_1 + \frac{4}{\pi}\gamma_0\sqrt{\gamma_1}$	$\frac{1}{\pi}\gamma_0^2 + \gamma_1 + \frac{64}{3\pi^2}\gamma_0\sqrt{\gamma_1}$
λ_2	$\frac{2}{\pi}(\gamma_0 + \gamma_1)^2$	$\frac{2}{\pi}\gamma_0^2 + 3\gamma_1 + \frac{8}{\pi}\gamma_0\sqrt{\gamma_1}$	$\frac{2}{\pi}\gamma_0^2 + 3\gamma_1 + \frac{128}{3\pi^2}\gamma_0\sqrt{\gamma_1}$
λ_3	$\frac{1}{\pi}(\gamma_0 + \gamma_1)^2$	$\frac{1}{\pi}\gamma_0^2 + \gamma_1 + \frac{4}{\pi}\gamma_0\sqrt{\gamma_1}$	$\frac{1}{\pi}\gamma_0^2 + 2\gamma_1 + \frac{64}{3\pi^2}\gamma_0\sqrt{\gamma_1}$
λ_4	$\gamma_0 + \gamma_1$	$\gamma_0 + 2\sqrt{\gamma_1}$	$\gamma_0 + \frac{32}{3\pi}\sqrt{\gamma_1}$
	PVT/PVT	PVT/PDT	PDT/PDT
λ_1	$2\gamma_0 + 2\gamma_1 + \frac{8}{\pi}\sqrt{\gamma_0\gamma_1}$	$2\gamma_0 + \gamma_1 + \frac{128}{3\pi^2}\sqrt{\gamma_0\gamma_1}$	$\gamma_0 + \gamma_1 + \frac{2048}{9\pi^3}\sqrt{\gamma_0\gamma_1}$
λ_2	$3\gamma_0 + 3\gamma_1 + \frac{16}{\pi}\sqrt{\gamma_0\gamma_1}$	$3\gamma_0 + 3\gamma_1 + \frac{256}{3\pi^2}\sqrt{\gamma_0\gamma_1}$	$3\gamma_0 + 3\gamma_1 + \frac{4096}{9\pi^3}\sqrt{\gamma_0\gamma_1}$
λ_3	$\gamma_0 + \gamma_1 + \frac{8}{\pi}\sqrt{\gamma_0\gamma_1}$	$\gamma_0 + 2\gamma_1 + \frac{128}{3\pi^2}\sqrt{\gamma_0\gamma_1}$	$2\gamma_0 + 2\gamma_1 + \frac{2048}{9\pi^3}\sqrt{\gamma_0\gamma_1}$
λ_4	$2\sqrt{\gamma_0} + 2\sqrt{\gamma_1}$	$2\sqrt{\gamma_0} + \frac{32}{3\pi}\sqrt{\gamma_1}$	$\frac{32}{3\pi}\sqrt{\gamma_0} + \frac{32}{3\pi}\sqrt{\gamma_1}$

Table 3. Distance values and model parameters for actin networks. Recall that parameters γ may have different meanings depending on the tessellation type (for PLT γ is given in nm/nm^2 , for PVT and PDT the unit for γ is $1/nm^2$).

Model	Distance	γ_0	γ_1	γ_1
Basic tessellations				
PLT	0.2496	$6.981 * 10^{-2}$	-	-
PVT	0.2534	$1.086 * 10^{-3}$	-	-
PDT	0.7369	$7.905 * 10^{-4}$	-	-
One-fold superpositions				
PLT/PLT	0.2496	$3.491 * 10^{-2}$	$3.491 * 10^{-2}$	-
PLT/PVT	0.0562	$2.167 * 10^{-2}$	$5.488 * 10^{-4}$	-
PLT/PDT	0.2467	$6.850 * 10^{-2}$	$1.168 * 10^{-7}$	-
PVT/PVT	0.0584	$2.920 * 10^{-4}$	$2.920 * 10^{-4}$	-
PVT/PDT	0.0322	$5.802 * 10^{-4}$	$4.116 * 10^{-5}$	-
PDT/PDT	0.3923	$1.254 * 10^{-4}$	$1.254 * 10^{-4}$	-
Two-fold superpositions				
PLT/PVT/PVT	0.0562	$1.680 * 10^{-2}$	$4.141 * 10^{-6}$	$5.447 * 10^{-4}$
PLT/PVT/PDT	0.0322	$7.105 * 10^{-14}$	$5.802 * 10^{-4}$	$4.116 * 10^{-5}$
PLT/PDT/PDT	0.2467	$6.850 * 10^{-2}$	$1.168 * 10^{-7}$	$5.317 * 10^{-15}$
PVT/PVT/PVT	0.0584	$5.4448 * 10^{-5}$	$2.789 * 10^{-5}$	$4.664 * 10^{-4}$
PVT/PVT/PDT	0.0322	$5.802 * 10^{-4}$	$4.253 * 10^{-27}$	$4.116 * 10^{-5}$
PVT/PDT/PDT	0.0322	$5.802 * 10^{-4}$	$5.351 * 10^{-30}$	$4.116 * 10^{-5}$
PDT/PDT/PDT	0.3277	$5.633 * 10^{-5}$	$5.633 * 10^{-5}$	$5.633 * 10^{-5}$

Figure legends

Figure 1: Single-layer tessellation models with the total length of edges being constant for all models.

Figure 1a: PLT

Figure 1b: PVT

Figure 1c: PDT

Figure 2: Actin filament network in lamellipodia of B16F1 mouse melanoma cells imaged by electron microscopy. Actual sample images are marked in white

Figure 3: Segmentation of actin filaments, original image and superimposed graph structure

Figure 4: Realizations of superposed tessellation models.

Figure 4a: PLT/PLT

Figure 4b: PLT/PVT

Figure 4c: PLT/PDT

Figure 4d: PVT/PVT

Figure 4e: PVT/PDT

Figure 4f: PDT/PDT

Figure 5: Comparison between segmented sample image and realization of optimal PVT/PDT superposed model fitted to actin networks.

Figure 6: Estimations of elasticity for actin networks with a mean mesh size of 34 nm (left panel) and 78 nm (right panel) and α -actinin concentrations between 5 and 25 μM .

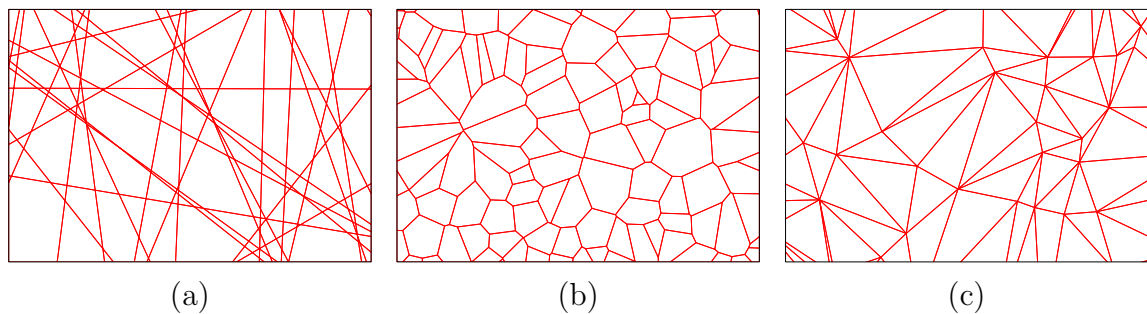


Figure 1.

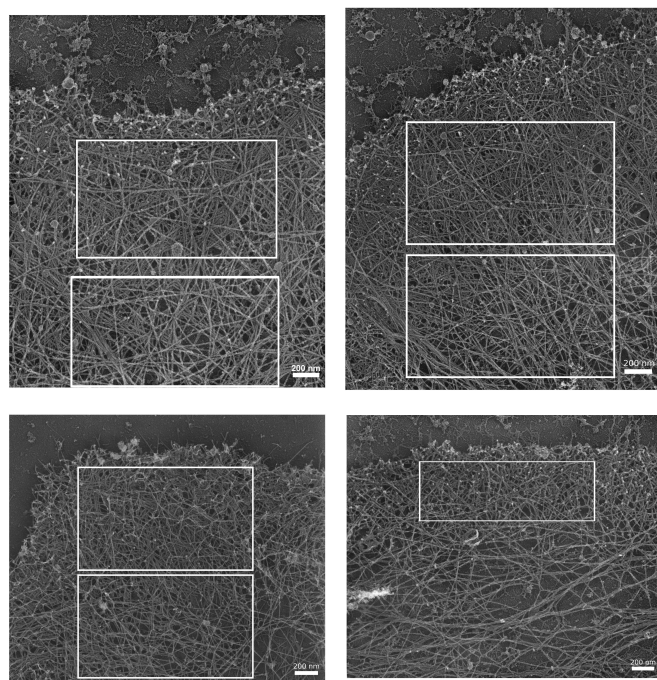


Figure 2.

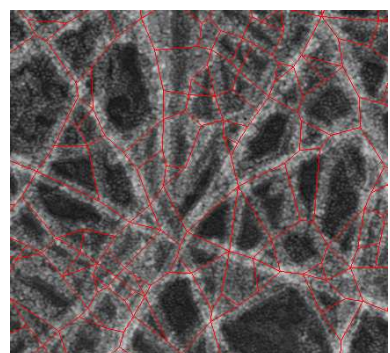


Figure 3.

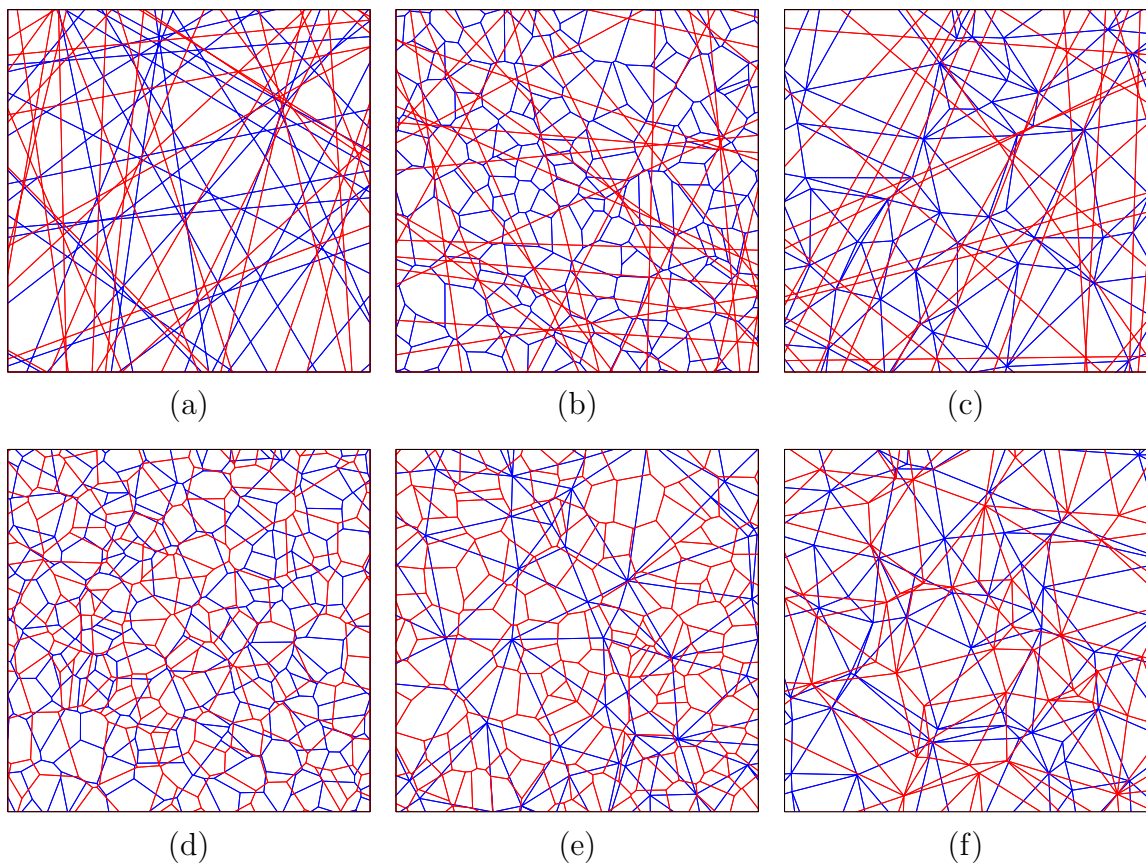


Figure 4.

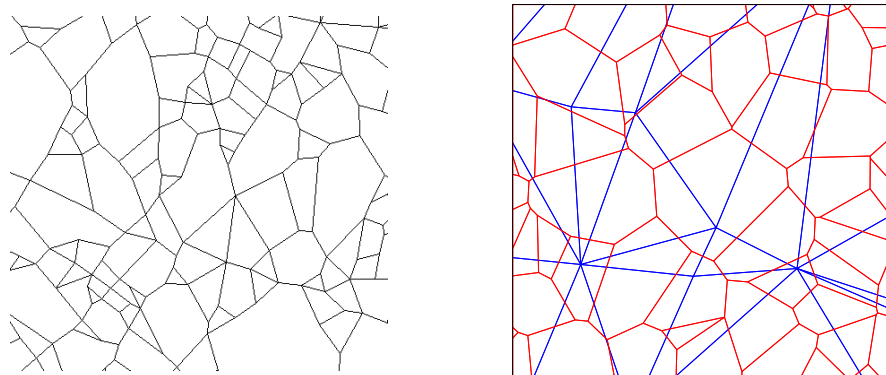


Figure 5.

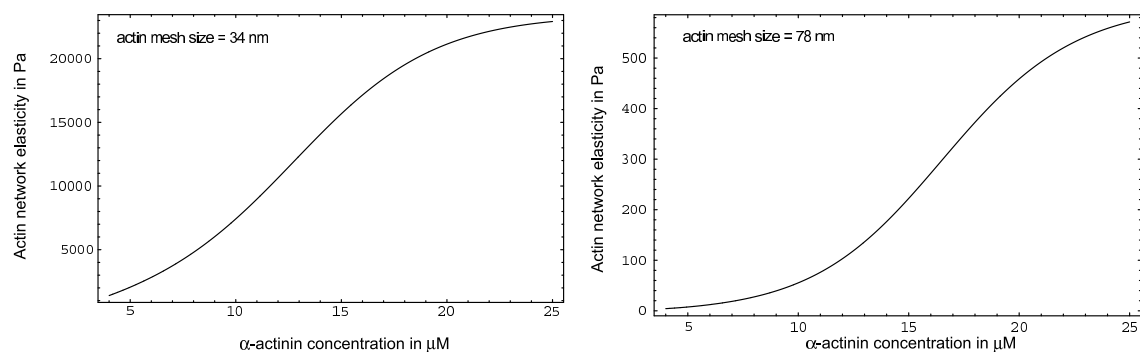


Figure 6.